

Traversing within the Gaussian Typical Set: Differentiable Gaussianization Layers for Inverse Problems Augmented by Normalizing Flows

Dongzhuo Li Huseyin Denli

ExxonMobil Research & Engineering Company, Annandale, NJ 08801, USA

{dongzhuo.li, huseyin.denli}@exxonmobil.com

Abstract

Generative networks such as normalizing flows can serve as a learning-based prior to augment inverse problems to achieve high-quality results. However, the latent space vector may not remain a typical sample from the desired high-dimensional standard Gaussian distribution when traversing the latent space during an inversion. As a result, it can be challenging to attain a high-fidelity solution, particularly in the presence of noise and inaccurate physics-based models. To address this issue, we propose to re-parameterize and Gaussianize the latent vector using novel differentiable data-dependent layers wherein custom operators are defined by solving optimization problems. These proposed layers enforce an inversion to find a feasible solution within a Gaussian typical set of the latent space. We tested and validated our technique on an image deblurring task and eikonal tomography – a PDE-constrained inverse problem and achieved high-fidelity results.

1. Introduction

Many scientific imaging problems are essentially inverse problems, which use observed data to infer properties of a physical system. For example, astrophysicists use radio electromagnetic data to image galaxies and black holes [1, 21]. Geoscientists use seismic recordings to reveal the internal structures of Earth [51, 52, 55]. Biomedical engineers and doctors use X-ray projections, ultrasound measurements, and magnetic resonance data to reconstruct images of human tissues and organs [17, 31, 37]. However, inverse problems are typically ill-posed with incomplete information provided by data, and thus there are infinitely many compatible solutions. Worse still, the observed data are usually noisy, and the assumed physics-based model may not be accurate. All these challenges require using regularization to inject *a priori* knowledge into inversion processes to obtain plausible results.

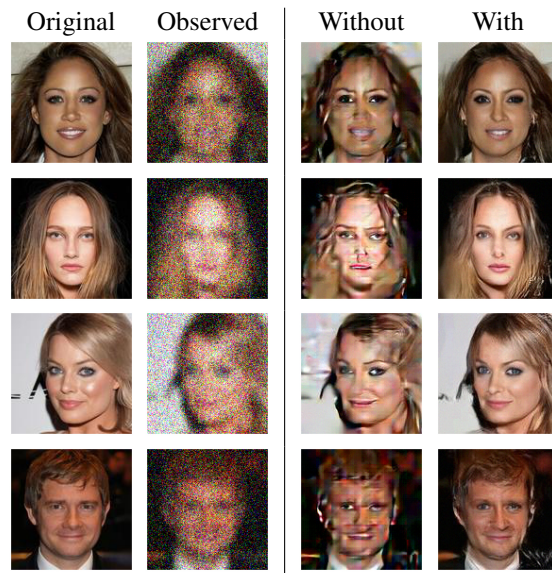


Figure 1. Comparison between normalization flow augmented inversion results (deblurring) with and without our proposed Gaussianization layers. The observed data are generated by blurring and adding strong noise to the original ones. Results obtained with the proposed layers have higher quality and much fewer artifacts.

Recently, deep-learning-based models have shown great promise for augmenting various inverse problems [3, 9, 20, 32, 36, 38, 42, 47, 50, 53, 54, 58, 59, 64]. In particular, deep generative models, such as VAEs [29], GANs [19], and normalizing flows [15, 16, 28, 48], which directly learn from training data distributions, are a powerful and versatile prior. Our work progresses from the prior art [3] that utilizes Glow [27] to augment inversion-based imaging problems, which demonstrates that normalizing flows are superior to other architectures such as GANs for such tasks.

Although normalizing flows are a very effective regularizer, we find that the quality of inversion results reduces significantly in the presence of noise and inaccurate physics-

based models (Figure 1). This is caused by the deviation of the latent vector from a typical sample from a standard Gaussian distribution, on which pre-trained normalizing flows are defined. The majority of probability mass of a high-dimensional distribution lies within a so-called typical set, which may not necessarily correspond to the region of the highest probability density of the prior or the posterior distributions. Typical samples from a high-dimensional distribution rarely reside outside this typical set. This issue has also been discussed in out-of-distribution (OOD) detection literatures (*e.g.*, [12, 41, 43, 44, 57]).

In this paper, we propose a set of differentiable Gaussianization layers to re-parameterize and Gaussianize the latent vectors of normalizing flows for inverse problems. These layers mainly consist of an orthogonal transformation that increases the statistical independence among latent vector components and nonlinear activation functions for (marginal) 1D Gaussianization. Although our technique is developed for normalizing flows, it can also be applied to other deep generative models.

The remainder of this article is organized as follows. Section 2 provides the background and mathematical statement of the problem. Section 3 introduces the Gaussianization layers, and Section 4 discusses related work. In Section 5, we first present both quantitative and qualitative results from a deblurring task on a downsampled CelebA-HQ dataset [25]. Then, we present an additional example from eikonal tomography. Section 6 discusses the limitations of this work and concludes the paper.

2. Background & Problem Statement

Suppose the forward mapping can be symbolically written as

$$\mathbf{d} = g(\mathbf{m}) + \epsilon, \quad (1)$$

where g stands for the physics-based model that can be governed by a partial differential equation (PDE), ϵ denotes noise, \mathbf{d} the observed data, and \mathbf{m} the physical parameters to be determined. In the augmented inversion framework, we solve the inverse problem by finding the maximum *a posteriori* (MAP) estimate from

$$p_M(\mathbf{m}|\mathbf{d}) \propto p(\mathbf{d}|\mathbf{m}) p_M(\mathbf{m}) \quad (2)$$

using gradient-based optimization methods, such as the conjugate gradient method or quasi-Newton methods. The probability density p_M introduces our *a priori* knowledge and is represented by a normalizing flow (Glow) f_θ , which is a differentiable invertible mapping between two distributions, parameterized by neural network parameters θ : $\mathbf{m} = f_\theta(\mathbf{z})$, where \mathbf{z} is the latent vector. After training,

the log probability density of a given model \mathbf{m} is

$$\begin{aligned} \log p_M(\mathbf{m}; \theta) &= \log p_Z(f_\theta^{-1}(\mathbf{m})) + \log \left| \det J_{f_\theta^{-1}}(\mathbf{m}) \right| \\ &= \log p_Z(\mathbf{z}) - \log \left| \det J_{f_\theta}(\mathbf{z}) \right|, \end{aligned} \quad (3)$$

where p_Z is the probability density function of a standard Gaussian distribution.

In an augmented inversion, we freeze the network weights; hence, we drop θ in f_θ hereafter in our notation. Therefore, the original inverse problem can be formulated in the following form, parameterized by a latent space representation:

$$\begin{aligned} \arg \min_{\mathbf{z}} \|\mathbf{d} - g \circ f(\mathbf{z})\|_2^2 \\ - \beta (\log p_Z(\mathbf{z}) - \log \left| \det J_f(\mathbf{z}) \right|), \end{aligned} \quad (4)$$

where β is a weighting factor. We can retrieve an inverted \mathbf{m} by a forward pass of mapping from an inverted \mathbf{z} . In all our experiments, we only use the additive coupling layer rather than the affine coupling layer since we observe instabilities with the latter, which is also mentioned in [5].

However, this formulation of augmented inversion leads to unsatisfactory results, as shown in Figure 1. In addition, if we put a large weight on the prior term, we also see strong artifacts, as shown in Figure 5.

In high-dimensional spaces, counterintuitively, the mass of a standard Gaussian distribution concentrates in a typical set [6, 14], which we refer to as the **Gaussian typical set** and give its formal definition in the supplementary materials. A well-trained normalizing flow maps samples from the target distribution into the Gaussian typical set with very high probability and vice versa (supplementary materials). Therefore, the normalizing flow may map atypical latent vectors to unrealistic images or physical parameters out of the target distribution.

Unfortunately, the latent vector can move outside the Gaussian typical set during inversion with formulation 4. For example, the MAP estimate may reside outside the typical set (*e.g.*, a very large β drives the latent vector towards the center), or in general the latent vector entries become non-i.i.d. Noises or inaccurate physics model assumptions would exacerbate this situation. Therefore, we need to constrain the latent vector within the Gaussian typical set during inversion.

3. Method

3.1. Re-parameterization with Gaussianization Layers

Our proposed solution is to re-parameterize the latent space vector \mathbf{z} by another random vector \mathbf{v} with differentiable layers that ‘‘Gaussianize’’ the inputs, such that $\mathbf{z} =$

$h(\mathbf{v}) \sim \mathcal{N}(\mathbf{0}, \mathbf{I})$, $\mathbf{v} \in \mathbb{R}^n$. The space of vector \mathbf{v} can be regarded as the latent space of the original latent space. In this deeper latent space, \mathbf{v} is unconstrained. Even if the optimization pushes \mathbf{v} out of the Gaussian typical set, the mapping h can shape it towards a typical example from the desired high-dimensional standard Gaussian distribution. Therefore, the original augmented inverse problem 4 becomes

$$\arg \min_{\mathbf{v}} \|\mathbf{d} - g \circ f \circ h(\mathbf{v})\|_2^2 - \beta (\log p_Z(h(\mathbf{v})) - \log |\det J_f(h(\mathbf{v}))|). \quad (5)$$

The Gaussianization layers keep the optimization problem unconstrained, enabling us to use highly efficient unconstrained optimizers, such as the L-BFGS solver [45].

Remark: It is also reasonable to use a maximum-likelihood formulation instead of the maximum *a posteriori* formulation in Problem 5 since the Gaussianization transformation imposes a hard constraint on latent vectors. For comparison purposes, we keep using the MAP formulation in our experiments.

Now the question is: what do we mean by requiring $\mathbf{z} = h(\mathbf{v}) \sim \mathcal{N}(\mathbf{0}, \mathbf{I})$ since there is only one realization in an inversion? The answer is to Gaussianize latent patches. Supposing that \mathbf{m} has a shape of $n_c \times n_x \times n_y$, the latent space tensor also has the same dimension. In addition, the latent tensors can be partitioned into non-overlapping patches of dimension $n_c \times w \times w$. We here make an assumption that the patch tensors are independent and identically distributed (i.i.d.), *i.e.*, the vectorized patch tensors $\mathbf{v}_i \in \mathbb{R}^D$ ($D = n_c \times w \times w$, $i = 1, \dots, N$) are i.i.d. random vectors.

The task now comes down to constructing a mapping $\mathbf{z}_i = h'(\mathbf{v}_i)$, such that $\mathbf{z}_i \sim \mathcal{N}(\mathbf{0}, \mathbf{I})$. As a result, the concatenation of \mathbf{z}_i , $i=1, \dots, N$ will also be a random vector \mathbf{z} distributed as a standard Gaussian. From a more tractable optimization perspective, we want to minimize $D_{\text{KL}}(\mathbf{z}_i \| \mathcal{N}(\mathbf{0}, \mathbf{I}))$, which can be decomposed as the sum of mutual information $I(\mathbf{z}_i)$ and marginal negentropy $J_m(\mathbf{z}_i)$ [11]:

$$D_{\text{KL}}(p(\mathbf{z}_i) \| \mathcal{N}(\mathbf{0}, \mathbf{I})) = I(\mathbf{z}_i) + J_m(\mathbf{z}_i), \quad (6)$$

where

$$I(\mathbf{z}_i) = D_{\text{KL}}\left(p(\mathbf{z}_i) \left\| \prod_j^D p_j(z_i^{(j)})\right.\right), \quad (7)$$

and

$$J_m(\mathbf{z}_i) = \sum_{j=1}^D D_{\text{KL}}\left(p_j(z_i^{(j)}) \left\| \mathcal{N}(0, 1)\right.\right). \quad (8)$$

Here $z_i^{(j)}$ denotes the j -th component of patch vector \mathbf{z}_i , and p_j stands for the marginal PDF for that component.

Taking advantage of the fact that the KL divergence and a standard Gaussian in Equation 6 are invariant to an orthogonal transformation and that the mutual information term is invariant to a component-wise invertible transformation, we propose to conduct the Gaussianization in the following steps, similar to [11, 30]:

1. Minimize the mutual information $I(\mathbf{z}_i)$ – making the components statistically independent. This is done by an orthogonal transformation that keeps the KL divergence the same but increases the negentropy $J_m(\mathbf{z}_i)$.
2. Minimize the marginal negentropy $J_m(\mathbf{z}_i)$ by component-wise operations that perform 1D Gaussianization of marginal distributions p_j , $j=1, \dots, D$. The mutual information does not change under component-wise invertible operations. Therefore, the overall KL divergence between \mathbf{z}_i and the Gaussian distribution decreases.

The orthogonal matrix and the nonlinear element-wise operations resemble neural network layers, but there are no extra parameters introduced. The nonlinear activation layers are data-dependent, and the outputs are obtained by solving optimization problems; therefore, special care should be taken to implement the gradient computation correctly and ensure that they pass the finite-difference convergence test (see the supplementary materials).

3.2. Reducing Mutual Information – ICA Layer

The orthogonal matrix \mathbf{W} is constructed by the independent component analysis. As we stated previously, patch vectors $\{\mathbf{v}_i\}$, $i=1, \dots, N$ from \mathbf{v} are assumed as i.i.d. random vectors; therefore, $\mathbf{p}_i = \mathbf{W}\mathbf{v}_i$ are also i.i.d. Besides, the orthogonal matrix \mathbf{W} makes the entries of each \mathbf{p}_i independent random variables. Therefore, the concatenated output random vector $\mathbf{p} = [\mathbf{p}_1, \mathbf{p}_2, \dots, \mathbf{p}_N]$ has independent components. The default patch size is 3 (or 1) $\times 8 \times 8$.

Our proposed layer to reduce mutual information is based on the FastICA algorithm [22, 24], which employs a fixed-point algorithm to maximize a contrast function Φ (*e.g.*, the logcosh function).

The FastICA algorithm typically requires that the data are pre-whitened. We adopt the iterative whitening method introduced in [22] (see supplementary materials). With whitened data, we compute \mathbf{W} using a damped fixed-point iteration scheme (\mathbf{w}_i is the i -th column vector of \mathbf{W}):

$$\mathbf{w}_i = \alpha \mathbb{E} [\mathbf{v} \phi(\mathbf{w}_i^\top \mathbf{v})] - \mathbb{E} [\phi'(\mathbf{w}_i^\top \mathbf{v})] \mathbf{w}_i, \quad (9)$$

or in the matrix form:

$$\mathbf{W} = \frac{1}{N} \left[\alpha \mathbf{V} \phi(\mathbf{W}^\top \mathbf{V})^\top - \mathbf{W} \text{diag}(\phi'(\mathbf{W}^\top \mathbf{V}) \mathbf{1}) \right], \quad (10)$$

where $\mathbf{1}$ is an all-one vector, $\phi(\cdot) = \Phi'(\cdot)$, $\alpha \in (0, 1)$, and we use $\alpha = 0.8$ throughout our experiments. To save computation time, we only perform a maximum of 10 iterations. The details of the whole algorithm can be found in the supplementary materials.

We set the initial \mathbf{W} as an identity matrix. If the input vectors are already i.i.d. Gaussian (within the Gaussian typical set), the computed \mathbf{W} will still be an identity matrix, which maps the input to the same output. This theoretical situation means that our ICA layer maps vectors in the Gaussian typical set to themselves. In practice, the empirical distribution from finite samples is not a standard Gaussian, so \mathbf{W} is not an identity matrix but another orthogonal matrix, which still maps i.i.d. standard Gaussian input vectors to i.i.d. standard Gaussian vectors. This corresponds to the fact that ICA cannot differentiate Gaussian sources, but our inversion application works fine with this case.

3.3. Reducing Marginal Negentropy

For 1D Gaussianization, we choose a combination of the Yeo-Johnson transformation that reduces skewness and the Lambert $W \times F_X$ transformation that reduces heavy-tailedness. Both of them are layers based on optimization. Each optimization problem in these transforms only depends on one parameter, which is cheap to compute and is easy to back-propagate the gradient. Equation 8 requires us to perform such 1D transformations for each component of the random vectors. In other words, we need to solve the same optimization problem for D times, which imposes a huge computational burden. Instead, we empirically find it acceptable to share the same optimization-generated parameter across all components; that is, we perform only a single 1D Gaussianization, treating all entry values in the latent vector as the data simultaneously.

Power Transformation Layer. We propose to use the power transformation or Yeo-Johnson transformation [60] to reduce the skewness of distributions:

$$s(\lambda, p) = \begin{cases} \left((p+1)^\lambda - 1 \right) / \lambda, & p \geq 0, \lambda \neq 0, \\ \log(p+1), & p \geq 0, \lambda = 0, \\ -\frac{(-p+1)^{2-\lambda}-1}{(2-\lambda)}, & p < 0, \lambda \neq 2, \\ -\log(-p+1), & p < 0, \lambda = 2, \end{cases} \quad (11)$$

where p is an input value, s is an output value, and λ is the parameter to be estimated. As shown in Figure 2(a), the form of the Yeo-Johnson activation function depends on parameter λ . If $\lambda = 1$, the mapping is an identity mapping. If $\lambda \geq 1$, the activation function is convex, which compresses the left tail and extends the right tail, reducing the left-skewness. If $\lambda \leq 1$, the activation function is concave, which oppositely reduces the right-skewness. The only parameter λ is determined by solving an optimization problem

that minimizes the negentropy:

$$\begin{aligned} \lambda &= \arg \max_{\lambda} l(\lambda | \mathbf{p}) \\ &= \arg \max_{\lambda} -\frac{n}{2} \log(\text{Var}(s(\lambda, p_i))) \\ &\quad + (\lambda - 1) \sum_{i=1}^n \text{sign}(p_i) \log(|p_i| + 1), \end{aligned} \quad (12)$$

where \mathbf{p} is an input data vector with entries $p_i, i=1, \dots, n$. We refer the readers to the supplementary materials for details in implementation and algorithm summary.

Lambert $W \times F_X$ Layer. Due to noise and inaccurate physics-based models, we observe that the distribution of latent vector values tends to be shaped as a heavy-tailed distribution during the inversion process. To reduce the heavy-tailedness, we adopt the Lambert $W \times F_X$ method detailed in [18].

Let X be a random variable whose CDF is F_X , with mean μ_X and standard deviation σ_X . The following transformation with a heavy-tail parameter $\delta \geq 0$:

$$S = \left(U \exp\left(\frac{\delta}{2} U^2\right) \right) \sigma_X + \mu_X, \quad (13)$$

where $U = (X - \mu_X) / \sigma_X$, is a bijection and maps X to another random variable S with heavier tails.

We use the parameterized Lambert $W \times F_X$ distribution family to approximate a heavy-tailed input and solve an optimization to estimate an optimal δ (see the supplementary materials), with which the inverse transformation maps to an output as Gaussian as possible.

Figure 2(b) shows that the Lambert $W \times F_X$ layer acts as a nonlinear squashing function. As δ increases, it compresses more the large values and reduces the heavy-tailedness. Intuitively, the Lambert $W \times F_X$ layer can also be interpreted as an intelligent way of imposing constraints on the range of values instead of a simple box constraint. We refer the readers to the supplementary materials for more details about the optimization problem and implementation.

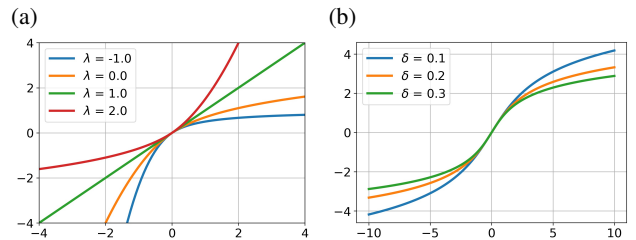


Figure 2. The nonlinear activation functions from (a) the power transformation (Yeo-Johnson) layer and (b) the Lambert $W \times F_X$ layer.

Standardization with Temperature. Since the output of the Lambert $W \times F_X$ Layer may not necessarily be zero mean and unit (or a prescribed) variance, we standardize the output using

$$z = (x - \mathbb{E}x) / \sqrt{\text{Var}(x)} * \gamma, \quad (14)$$

where γ is the temperature parameter suggested in [27].

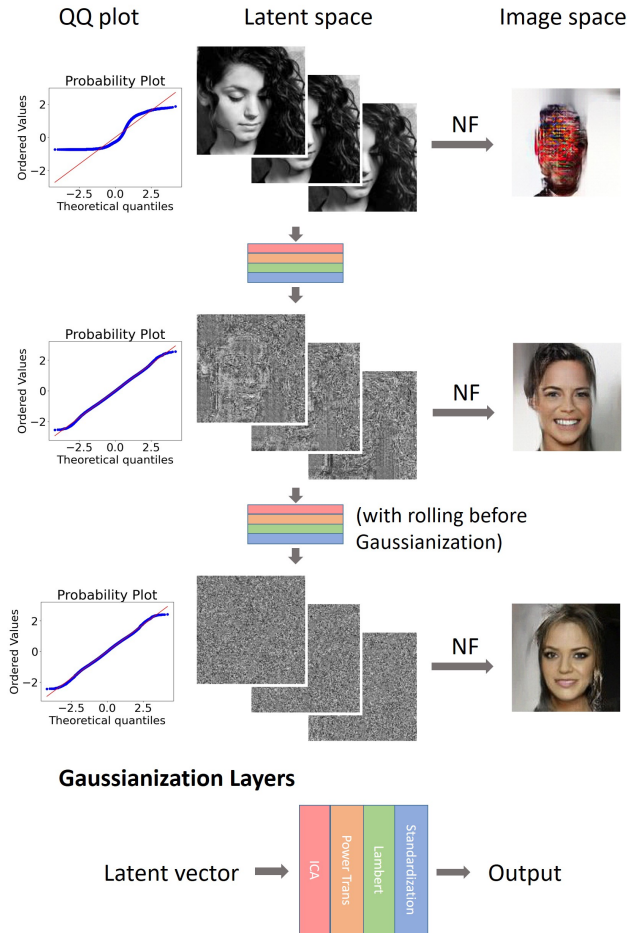


Figure 3. The effects of Gaussianization layers. As an exaggerated example, we use a standardized (with the temperature as 0.8) image as a latent tensor. The latent tensor components are not independent, and the values of latent tensor do not follow a Gaussian distribution as indicated by the QQ-plot. Then, we apply the proposed Gaussianization layers twice, which destroy the patterns and make the values approximately distributed as a Gaussian with a temperature of 0.8. After only one pass, the image output using the normalizing flow becomes plausible. In fact, only one set of these layers are adequate for inversion. We talk about the rolling operation in the supplementary materials.

In summary, we illustrate the effects of the Gaussianization layers in Figure 3, which shows that these layers eliminate latent space patterns, *i.e.*, making latent pixels indepen-

dent, and shape their value distribution towards an isotropic Gaussian distribution (with a given temperature).

4. Related Work

Gaussianization. Chen and Gopinath [11] proposed an EM algorithm to iteratively Gaussianize high-dimensional data. The rotation-based iterative Gaussianization (RBIG) method [30] consists of iterations of a marginal Gaussianization transformation and an orthogonal transformation. These methods laid the foundation for our strategy: an orthogonal transformation to minimize mutual information and 1D Gaussianization transformations to minimize marginal negentropy. Meng *et al.* [40] proposed a normalizing flow named the Gaussianization flow based on the same strategy. Their 1D Gaussianization transformation resembles the one in [11], where they use kernel density estimation (KDE) with learnable parameters (*i.e.*, 20 to 100 anchor point locations and bandwidths) to approximate the CDF and apply inverse CDF transformation to map data to a Gaussian. This approach also inspired us to experiment with the same parameterization in our optimization-based layers. However, we found it hard to obtain a non-singular Hessian for backward propagation of gradients and at the same time achieve good forward Gaussianization performance. Also, the computation cost for this approach is higher than our single-parameter optimization. We also would like to acknowledge that the “latent space normalization” trick in the super-resolution normalization flow – SRFlow [35], a method for end-to-end super-resolution, inspired us to design Gaussianization layers to regularize inverse problems.

Implicit Layers. In contrast to traditional feed-forward neural network layers, implicit layers like OptNet [2] and the deep-equilibrium networks [4] compute the output either by solving an optimization problem or finding the solution to a nonlinear equation. Their gradient computation is similar to the adjoint-state method in computational physics, where automatic differentiation can be used to compute a vector-Jacobian product. More details and examples can be found in [39].

5. Experiments

5.1. Deconvolution with Noise and Inaccurate Kernel

We first tested our method on a deconvolution (deblurring) task. The inverse problem is to recover high-resolution images given blurred observations with possible noises, assuming we have a good knowledge of the smoothing kernel. Deconvolution has wide applications in image deblurring, astronomical imaging, and geophysical inversion. In our experiments, we use an isotropic Gaussian smoothing kernel G parameterized by its standard deviation τ . The math-

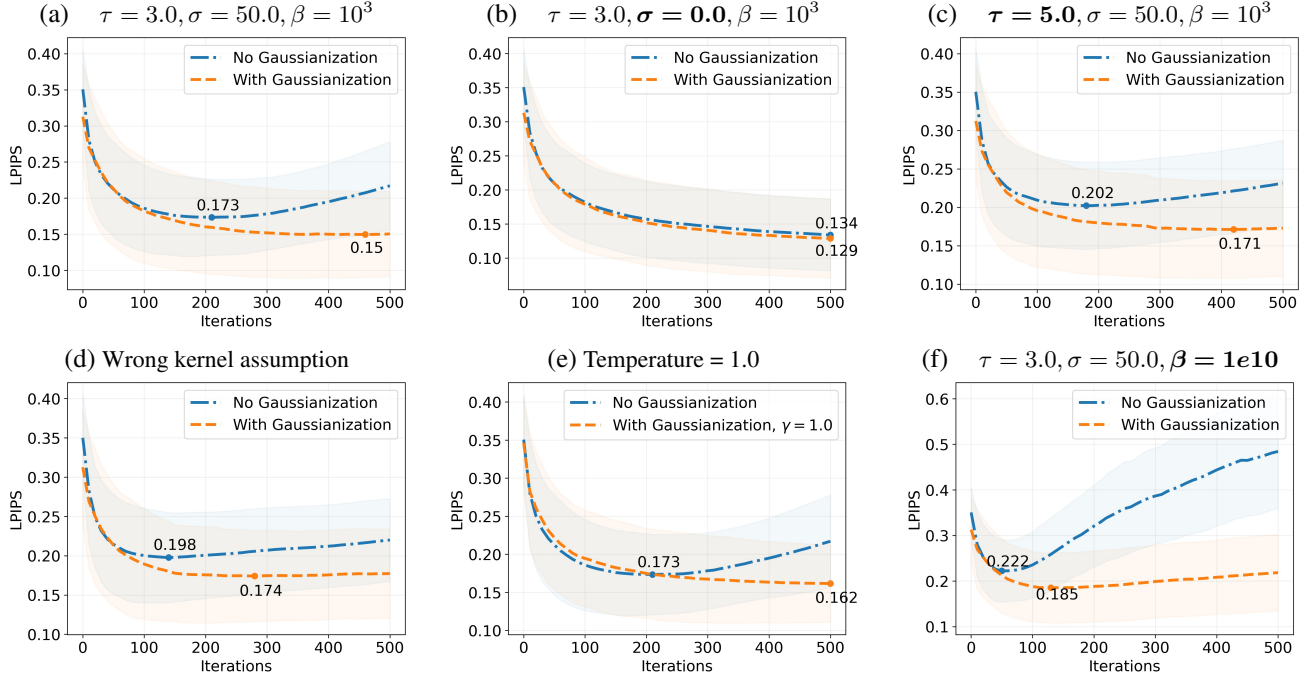


Figure 4. Summary of the metrics of inversion results with different parameters. A lower LPIPS value indicates a smaller restoration error. (a) Base case; (b) No added noise; (c) Heavier smoothing; (d) Inversion with a wrong smoothing kernel: the true $\tau = 3$, but we used $\tau = 5$ for inversion; (e) Inversion with a different temperature $\gamma = 1.0$; (f) Large β on the regularization term.

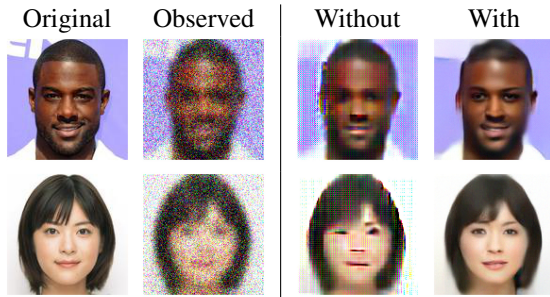


Figure 5. Comparison of inversion results with a large $\beta = 1e10$, which places a large weight on the regularization term. Without the Gaussianization layers, the latent vectors deviate from the Gaussian typical set, leading to strange artifacts.

emational formulation of the forward process is as follows

$$\mathbf{d} = G * \mathbf{m} + \epsilon, \quad (15)$$

where ϵ is added noise, and $*$ is the convolution operator. In our experiments, we assume that $\epsilon \sim \mathcal{N}(\mathbf{0}, \sigma^2 \mathbf{I})$. This ill-posed problem is especially challenging when the noise is strong or the smoothing kernel estimate is inaccurate.

We used the CelebA-HQ dataset [25] (under the Creative Commons CC BY-NC 4.0 license) for testing and evaluation. All images were downsampled to the resolution of 128×128 . We trained the Glow network with the original

training-validation-testing split configuration as the CelebA dataset [34] (see the supplementary materials). For the inversion tests, we randomly selected 100 images from the test set. All inversions started with the same Gaussian random vector in the latent space.

There are two parameters for experiments: the standard deviation of the Gaussian smoothing kernel τ and the standard deviation of the added Gaussian noise σ . Besides, there are also two hyper-parameters for the inversion: the weighting parameter β from Problem 5 and the temperature γ of the latent space Gaussian.

We set the base case with $\tau = 3.0, \sigma = 50.0, \beta = 1000.0, \gamma = 0.7$ (β seems large because the prior term unit is bits-per-dimension). For comparison, we also changed each of these parameters one at a time to investigate their impact on inversion results. LPIPS [62] is the primary metric in our study to measure the similarity between the deconvolved results and the ground truth because it is closer to human perception than other metrics such as PSNR and SSIM [56]. Figure 4 summarizes the quantitative evaluation results at each inversion step, where we plot the averaged LPIPS metric curve and the standard deviation in the shaded area. In addition, we report the minimum mean values on the LPIPS curves. In all cases, our Gaussianization layers, on the one hand, enable inversions to achieve a lower restoration error, and on the other hand, keep results plausible throughout the entire inversion processes.

5.2. Ablation Study

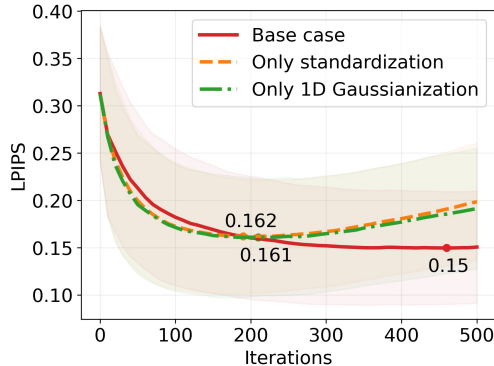


Figure 6. Ablation study. The results indicate that the ICA layer plays the most critical role in improving inversion results. The temperature was set to 0.7 in all cases.

We performed an ablation study to investigate the contribution from the components of the proposed Gaussianization layers. We first removed the ICA layer: we only kept the 1D Gaussianization layers (power transformation and Lambert $W \times F_X$) and the last standardization layer with a temperature of 0.7. Compared with the base case with Gaussianization layers, the minimum LPIPS increases from 0.15 to 1.61. The LPIPS curve also moves up as inversion continues, which means that the latent vectors of the deblurred images are getting out of the Gaussian typical set. Despite their inability to keep the LPIPS curve from going up, the 1D Gaussianization layers with standardization are able to reduce the minimum LPIPS compared with the base case without any part of Gaussianization layers (0.173).

We then removed all but the last standardization layer with a temperature of 0.7. The minimum LPIPS increases slightly from 1.61 to 1.62, suggesting the marginal improvement from only adding the power transformation and Lambert $W \times F_X$ layers. Considering both ablative procedures, it is clear that the ICA layer has the most significant contribution to keep results meaningful throughout inversion.

5.3. Eikonal Tomography

In this section, we perform tests on a highly ill-posed tomography problem where the physics phenomenon is described by a nonlinear PDE. The task of tomography is to use data recorded at the boundary of an object to reconstruct its internal structures. In acoustic wave imaging, the following eikonal equation approximately describes the shortest travel time $T(\mathbf{x}; \mathbf{x}_s)$ that the acoustic wave emerging from source location \mathbf{x}_s takes to reach location \mathbf{x} [61]:

$$\begin{aligned} |\nabla T(\mathbf{x}; \mathbf{x}_s)| &= \frac{1}{c(\mathbf{x})}, \quad \mathbf{x} \in \mathbb{R}^2 \\ T(\mathbf{x}_s; \mathbf{x}_s) &= 0, \end{aligned} \quad (16)$$

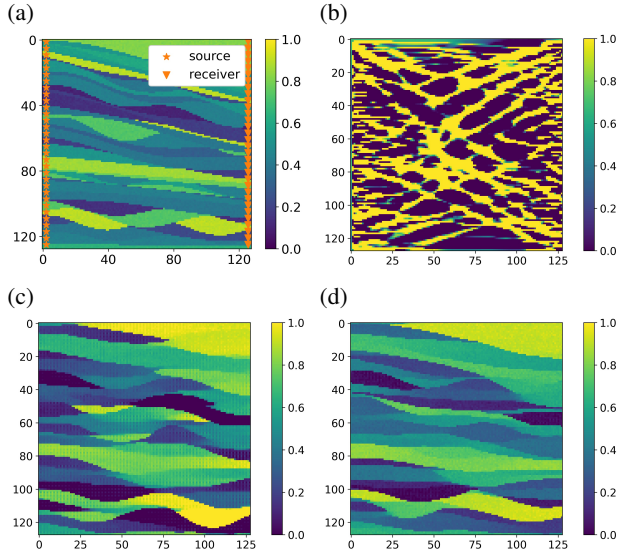


Figure 7. Comparison of results from eikonal tomography. (a) The true physical parameters and the source-receiver configuration. This represents a generic tomography setup; (b) Inversion results with traditional total variation regularization, where the result is blown up by noise; (c) Augmented inversion without Gaussianization layers, where grid-like artifacts exist; (d) Augmented inversion with Gaussianization layers, where the result has the highest quality.

where $c(\mathbf{x})$ is the wave propagation speed at each location. The goal is to reconstruct $c(\mathbf{x})$. Figure 7(a) shows the experiment setup where we placed sources at the left boundary and receivers at the right one. We excited waves from each source and recorded travel time at the receiver array, which constituted the observed data. We solved the eikonal equation using the fast sweeping method [63] and computed the gradient using the discrete adjoint-state method [33].

We used 100 randomly selected model parameters $m(\mathbf{x})$ from the test set for inversion, and Figure 7(a) shows one typical example. For simplicity, the parameter values were defined between 0 and 1 and then converted to $c(\mathbf{x})$ by the formula: $c(\mathbf{x}) = 100 m(\mathbf{x}) + 1500$, which was hence used in the forward physics model.

A good starting model $m_0(\mathbf{x})$ is necessary for this type of inversion with nonlinear physics-based models. In our synthetic tests, we obtained it by smoothing $m(\mathbf{x})$ by a Gaussian kernel with a standard deviation of 5. Then we found its projection in the latent space and started inversion from there. More details can be found in the supplementary materials.

We added noise to the recorded travel time using the following formula: $T_{\text{noisy}}(\mathbf{x}_r; \mathbf{x}_s) = T(\mathbf{x}_r; \mathbf{x}_s)(1 + \epsilon)$, where $\epsilon \sim \mathcal{N}(0, \sigma^2)$ and \mathbf{x}_r denotes any receiver location. In other words, a longer travel time corresponds to larger uncertainties.

With the projected latent vectors obtained with and without Gaussianization layers, we conducted inversion by solving Problem 4 and Problem 5, respectively. As an additional comparison, we did a conventional eikonal tomography inversion without the augmentation from a normalizing flow, but with the total variation regularization and a box constraint to force values to stay in $[0, 1]$. Figure 7 shows a qualitative comparison of inversion results when $\sigma = 0.1$. In augmented inversions, we set weighting parameter $\beta = 0.001$ and temperature $\gamma = 1.0$ in both cases with and without the Gaussianization layers. Comparing Figures 7(c) and 7(d), we see that the result with the Gaussianization layers has no mesh-like artifacts and stays within a more accurate value range.

Table 1 summarizes the best average metrics (LPIPS and SSIM) from inversions with 100 examples, with different noise levels σ and different β . This comparison favors inversions without the proposed layers since we are comparing the best results attained during the whole inversion process. Still, in almost all cases, inversion using our Gaussianization layers (the “on” cases) outperforms that without such layers (the “off” cases). Finally, we show in Figure 8 that if β is set too large as 0.1, the inverted wave speed parameters without the Gaussianization layers diverge to unrealistic results.

Table 1. The best average metrics from inversions with 100 randomly selected images from the test set, with different noise levels and weighting factor β . Inversion with our proposed layers achieves better numerical metrics in almost all scenarios.

| | β | $\sigma = 0.0025$ | | $\sigma = 0.005$ | | $\sigma = 0.01$ | |
|--------------------|-----------|-------------------|-------|------------------|-------|-----------------|-------|
| | | off | on | off | on | off | on |
| SSIM \uparrow | 10^{-5} | 0.443 | 0.437 | 0.366 | 0.368 | 0.291 | 0.295 |
| | 10^{-3} | 0.439 | 0.440 | 0.366 | 0.369 | 0.290 | 0.297 |
| | 10^{-1} | 0.312 | 0.375 | 0.329 | 0.372 | 0.289 | 0.294 |
| LPIPS \downarrow | 10^{-5} | 0.184 | 0.177 | 0.213 | 0.198 | 0.247 | 0.228 |
| | 10^{-3} | 0.185 | 0.175 | 0.212 | 0.201 | 0.251 | 0.228 |
| | 10^{-1} | 0.293 | 0.216 | 0.260 | 0.202 | 0.257 | 0.232 |

6. Discussion & Conclusions

We point out some limitations of this work. First, traversing within the Gaussian typical set means that the statistics of the training dataset will dominate the results. Figure 9 shows that our method cannot restore the eyeglasses because it is not a significant feature within our training data. One needs to pay particular attention to training dataset construction to ensure that it represents the typical features to be investigated. One should also interpret their results with this caveat in mind. Second, the Gaus-

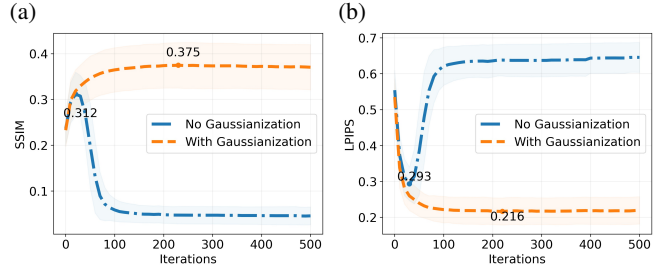


Figure 8. Comparison of eikonal tomography results with a large β (0.1) during the inversion process. (a) SSIM; (b) LPIPS. Without the Gaussianization layers, the inverted physical parameters diverge to unrealistic results.



Figure 9. A failure example where inversion is not able to restore the eyeglasses because of the strong constraint of traversing within the Gaussian typical set. The results are dominated by the bias of the training dataset.

sianization layers are based on optimization and fixed-point iterations, which can be computationally expensive. With one V100 GPU and an Intel Xeon Platinum 8276 CPU, it takes around 1.95 ± 0.30 seconds and 1.18 ± 0.21 seconds to finish one forward computation and one custom gradient back-propagation, respectively. The computation time was estimated by 1000 repeated experiments, and our implementation was in PyTorch. Nevertheless, the additional computation time is acceptable if the physics simulation part takes a much longer time. Third, our algorithm depends on the i.i.d. assumption about latent patches, which may not be valid since neighboring pixels from different patches may not be independent. Still, our method works well in practice and we also have designed the rolling operation (see supplementary materials) that shifts the patch extraction locations to improve independence if necessary.

In summary, we have proposed a set of Gaussianization layers: the ICA layer, the power transformation layer, the Lambert $W \times F_X$ layer, and the final standardization layer that are sequentially stacked together to re-parameterize and Gaussianize latent vectors for inverse problems augmented by deep generative priors (normalizing flows). These layers approximately keep the latent vector traversing within the Gaussian typical set in which the majority of latent-space probability mass concentrates and to which the target distribution corresponds. We have demonstrated the advantages of our proposed layers on two typical inverse problems from computational imaging.

References

- [1] Kazunori Akiyama, Antxon Alberdi, Walter Alef, Keiichi Asada, Rebecca Azulay, Anne-Kathrin Baczko, David Ball, Mislav Baloković, John Barrett, Dan Bintley, et al. First m87 event horizon telescope results. iv. imaging the central supermassive black hole. *The Astrophysical Journal Letters*, 875(1):L4, 2019. [1](#)
- [2] Brandon Amos and J Zico Kolter. Optnet: Differentiable optimization as a layer in neural networks. In *International Conference on Machine Learning*, pages 136–145. PMLR, 2017. [5](#)
- [3] Muhammad Asim, Max Daniels, Oscar Leong, Ali Ahmed, and Paul Hand. Invertible generative models for inverse problems: mitigating representation error and dataset bias. In *International Conference on Machine Learning*, pages 399–409. PMLR, 2020. [1](#)
- [4] Shaojie Bai, J. Zico Kolter, and Vladlen Koltun. Deep equilibrium models. In *Advances in Neural Information Processing Systems (NeurIPS)*, 2019. [5](#)
- [5] Jens Behrmann, Paul Vicol, Kuan-Chieh Wang, Roger Grosse, and Jörn-Henrik Jacobsen. Understanding and mitigating exploding inverses in invertible neural networks. In *International Conference on Artificial Intelligence and Statistics*, pages 1792–1800. PMLR, 2021. [2](#)
- [6] Michael Betancourt. A conceptual introduction to hamiltonian monte carlo. *arXiv preprint arXiv:1701.02434*, 2017. [2](#)
- [7] Avrim Blum, John Hopcroft, and Ravindran Kannan. *Foundations of data science*. Cambridge University Press, 2020. [15](#)
- [8] Piotr Bojanowski, Armand Joulin, David Lopez-Paz, and Arthur Szlam. Optimizing the latent space of generative networks. *arXiv preprint arXiv:1707.05776*, 2017. [16](#)
- [9] Ashish Bora, Ajil Jalal, Eric Price, and Alexandros G Dimakis. Compressed sensing using generative models. In *International Conference on Machine Learning*, pages 537–546. PMLR, 2017. [1](#)
- [10] Richard P Brent. *Algorithms for minimization without derivatives*. Courier Corporation, 2013. [13](#)
- [11] Scott Chen and Ramesh Gopinath. Gaussianization. *Advances in neural information processing systems*, 13:423–429, 2000. [3](#), [5](#)
- [12] Hyunsun Choi, Eric Jang, and Alexander A Alemi. Waic, but why? generative ensembles for robust anomaly detection. *arXiv preprint arXiv:1810.01392*, 2018. [2](#)
- [13] Robert M Corless, Gaston H Gonnet, David EG Hare, David J Jeffrey, and Donald E Knuth. On the lambertw function. *Advances in Computational mathematics*, 5(1):329–359, 1996. [13](#)
- [14] Thomas M Cover and Joy A Thomas. *Elements of Information Theory*. Wiley, 2012. [2](#), [12](#)
- [15] Laurent Dinh, David Krueger, and Yoshua Bengio. Nice: Non-linear independent components estimation. *arXiv preprint arXiv:1410.8516*, 2014. [1](#)
- [16] Laurent Dinh, Jascha Sohl-Dickstein, and Samy Bengio. Density estimation using real nvp. *arXiv preprint arXiv:1605.08803*, 2016. [1](#)
- [17] H Gemmeke and NV Ruiters. 3d ultrasound computer tomography for medical imaging. *Nuclear Instruments and Methods in Physics Research Section A: Accelerators, Spectrometers, Detectors and Associated Equipment*, 580(2):1057–1065, 2007. [1](#)
- [18] Georg M Goerg. The lambert way to gaussianize heavy-tailed data with the inverse of tukey’sh transformation as a special case. *The Scientific World Journal*, 2015, 2015. [4](#), [13](#), [14](#)
- [19] Ian J Goodfellow, Jean Pouget-Abadie, Mehdi Mirza, Bing Xu, David Warde-Farley, Sherjil Ozair, Aaron Courville, and Yoshua Bengio. Generative adversarial networks. *arXiv preprint arXiv:1406.2661*, 2014. [1](#)
- [20] Paul Hand, Oscar Leong, and Vladislav Voroninski. Phase retrieval under a generative prior. *arXiv preprint arXiv:1807.04261*, 2018. [1](#)
- [21] JA Högbom. Aperture synthesis with a non-regular distribution of interferometer baselines. *Astronomy and Astrophysics Supplement Series*, 15:417, 1974. [1](#)
- [22] Aapo Hyvärinen. Fast and robust fixed-point algorithms for independent component analysis. *IEEE transactions on Neural Networks*, 10(3):626–634, 1999. [3](#), [12](#)
- [23] Aapo Hyvärinen. The fixed-point algorithm and maximum likelihood estimation for independent component analysis. *Neural Processing Letters*, 10(1):1–5, 1999. [12](#)
- [24] Aapo Hyvärinen and Erkki Oja. Independent component analysis: algorithms and applications. *Neural networks*, 13(4-5):411–430, 2000. [3](#), [13](#)
- [25] Tero Karras, Timo Aila, Samuli Laine, and Jaakko Lehtinen. Progressive growing of gans for improved quality, stability, and variation. In *ICLR*, 2018. [2](#), [6](#)
- [26] Diederik Kingma and Jimmy Ba. Adam, a method for stochastic optimization. In *ICLR*, 2015. [14](#)
- [27] Diederik P Kingma and Prafulla Dhariwal. Glow: Generative flow with invertible 1x1 convolutions. *arXiv preprint arXiv:1807.03039*, 2018. [1](#), [5](#)
- [28] Diederik P Kingma, Tim Salimans, Rafal Jozefowicz, Xi Chen, Ilya Sutskever, and Max Welling. Improving variational inference with inverse autoregressive flow. *arXiv preprint arXiv:1606.04934*, 2016. [1](#)
- [29] Diederik P Kingma and Max Welling. Auto-encoding variational bayes. *arXiv preprint arXiv:1312.6114*, 2013. [1](#)
- [30] Valero Laparra, Gustavo Camps-Valls, and Jesús Malo. Iterative gaussianization: from ica to random rotations. *IEEE transactions on neural networks*, 22(4):537–549, 2011. [3](#), [5](#)
- [31] Paul C Lauterbur. Image formation by induced local interactions: examples employing nuclear magnetic resonance. *nature*, 242(5394):190–191, 1973. [1](#)
- [32] Dongzhuo Li, Huseyin Denli, Cody MacDonald, Kyle Basler-Reeder, Anatoly Baumstein, and Jacquelyn Daves. Multiparameter geophysical reservoir characterization augmented by generative networks. In *First International Meeting for Applied Geoscience & Energy*, pages 1364–1368. Society of Exploration Geophysicists, 2021. [1](#)
- [33] Dongzhuo Li, Kailai Xu, Jerry M Harris, and Eric Darve. Coupled time-lapse full-waveform inversion for subsurface flow problems using intrusive automatic differentiation. *Water Resources Research*, 56(8):e2019WR027032, 2020. [7](#)

- [34] Ziwei Liu, Ping Luo, Xiaogang Wang, and Xiaoou Tang. Deep learning face attributes in the wild. In *Proceedings of International Conference on Computer Vision (ICCV)*, December 2015. 6, 14
- [35] Andreas Lugmayr, Martin Danelljan, Luc Van Gool, and Radu Timofte. Srflow: Learning the super-resolution space with normalizing flow. In *European Conference on Computer Vision*, pages 715–732. Springer, 2020. 5
- [36] Sebastian Lunz, Ozan Öktem, and Carola-Bibiane Schönlieb. Adversarial regularizers in inverse problems. *arXiv preprint arXiv:1805.11572*, 2018. 1
- [37] Michael Lustig, David Donoho, and John M Pauly. Sparse mri: The application of compressed sensing for rapid mr imaging. *Magnetic Resonance in Medicine: An Official Journal of the International Society for Magnetic Resonance in Medicine*, 58(6):1182–1195, 2007. 1
- [38] Morteza Mardani, Enhao Gong, Joseph Y Cheng, Shreyas S Vasanaawala, Greg Zaharchuk, Lei Xing, and John M Pauly. Deep generative adversarial neural networks for compressive sensing mri. *IEEE transactions on medical imaging*, 38(1):167–179, 2018. 1
- [39] Joaquim RRA Martins and Andrew Ning. *Engineering design optimization*. Cambridge University Press, 2021. 5
- [40] Chenlin Meng, Yang Song, Jiaming Song, and Stefano Ermon. Gaussianization flows. In *International Conference on Artificial Intelligence and Statistics*, pages 4336–4345. PMLR, 2020. 5
- [41] Warren Morningstar, Cusuh Ham, Andrew Gallagher, Balaji Lakshminarayanan, Alex Alemi, and Joshua Dillon. Density of states estimation for out of distribution detection. In Arindam Banerjee and Kenji Fukumizu, editors, *Proceedings of The 24th International Conference on Artificial Intelligence and Statistics*, volume 130 of *Proceedings of Machine Learning Research*, pages 3232–3240. PMLR, 13–15 Apr 2021. 2
- [42] Lukas Mosser, Olivier Dubrule, and Martin J Blunt. Stochastic seismic waveform inversion using generative adversarial networks as a geological prior. *Mathematical Geosciences*, 52(1):53–79, 2020. 1
- [43] Eric Nalisnick, Akihiro Matsukawa, Yee Whye Teh, Dilan Gorur, and Balaji Lakshminarayanan. Do deep generative models know what they don’t know? In *ICLR*, 2019. 2
- [44] Eric Nalisnick, Akihiro Matsukawa, Yee Whye Teh, and Balaji Lakshminarayanan. Detecting out-of-distribution inputs to deep generative models using a test for typicality. *arXiv preprint arXiv:1906.02994*, 5:5, 2019. 2
- [45] Jorge Nocedal and Stephen Wright. *Numerical optimization*. Springer Science & Business Media, 2006. 3
- [46] Erkki Oja and Zhijian Yuan. The fastica algorithm revisited: Convergence analysis. *IEEE transactions on Neural Networks*, 17(6):1370–1381, 2006. 13
- [47] Gregory Ongie, Ajil Jalal, Christopher A Metzler, Richard G Baraniuk, Alexandros G Dimakis, and Rebecca Willett. Deep learning techniques for inverse problems in imaging. *IEEE Journal on Selected Areas in Information Theory*, 1(1):39–56, 2020. 1
- [48] George Papamakarios, Theo Pavlakou, and Iain Murray. Masked autoregressive flow for density estimation. *arXiv preprint arXiv:1705.07057*, 2017. 1, 16
- [49] Youcef Saad and Martin H Schultz. Gmres: A generalized minimal residual algorithm for solving nonsymmetric linear systems. *SIAM Journal on scientific and statistical computing*, 7(3):856–869, 1986. 15
- [50] Ali Siahkoochi, Gabrio Rizzuti, Mathias Louboutin, Philipp A Witte, and Felix J Herrmann. Preconditioned training of normalizing flows for variational inference in inverse problems. *arXiv preprint arXiv:2101.03709*, 2021. 1
- [51] Albert Tarantola. Inversion of seismic reflection data in the acoustic approximation. *Geophysics*, 49(8):1259–1266, 1984. 1
- [52] Jeroen Tromp, Carl Tape, and Qinya Liu. Seismic tomography, adjoint methods, time reversal and banana-doughnut kernels. *Geophysical Journal International*, 160(1):195–216, 2005. 1
- [53] Dmitry Ulyanov, Andrea Vedaldi, and Victor Lempitsky. Deep image prior. In *Proceedings of the IEEE conference on computer vision and pattern recognition*, pages 9446–9454, 2018. 1
- [54] Dave Van Veen, Ajil Jalal, Mahdi Soltanolkotabi, Eric Price, Sriram Vishwanath, and Alexandros G Dimakis. Compressed sensing with deep image prior and learned regularization. *arXiv preprint arXiv:1806.06438*, 2018. 1
- [55] Jean Virieux and Stéphane Operto. An overview of full-waveform inversion in exploration geophysics. *Geophysics*, 74(6):WCC1–WCC26, 2009. 1
- [56] Zhou Wang, Alan C Bovik, Hamid R Sheikh, and Eero P Simoncelli. Image quality assessment: from error visibility to structural similarity. *IEEE transactions on image processing*, 13(4):600–612, 2004. 6
- [57] Ziyu Wang, Bin Dai, David Wipf, and Jun Zhu. Further analysis of outlier detection with deep generative models. In Jessica Zosa Forde, Francisco Ruiz, Melanie F Pradier, and Aaron Schein, editors, *Proceedings on "I Can't Believe It's Not Better!" at NeurIPS Workshops*, volume 137 of *Proceedings of Machine Learning Research*, pages 11–20. PMLR, 12 Dec 2020. 2
- [58] Jay Whang, Qi Lei, and Alex Dimakis. Solving inverse problems with a flow-based noise model. In *Proceedings of the 38th International Conference on Machine Learning*, volume 139 of *Proceedings of Machine Learning Research*, pages 11146–11157. PMLR, 18–24 Jul 2021. 1
- [59] Yulang Wu and George A McMechan. Parametric convolutional neural network-domain full-waveform inversion. *Geophysics*, 84(6):R881–R896, 2019. 1
- [60] In-Kwon Yeo and Richard A Johnson. A new family of power transformations to improve normality or symmetry. *Biometrika*, 87(4):954–959, 2000. 4
- [61] Özdoğan Yilmaz. *Seismic data analysis*, volume 1. Society of exploration geophysicists Tulsa, 2001. 7
- [62] Richard Zhang, Phillip Isola, Alexei A Efros, Eli Shechtman, and Oliver Wang. The unreasonable effectiveness of deep features as a perceptual metric. In *CVPR*, 2018. 6

- [63] Hongkai Zhao. A fast sweeping method for eikonal equations. *Mathematics of computation*, 74(250):603–627, 2005. [7](#)
- [64] Weiqiang Zhu, Kailai Xu, Eric Darve, Biondo Biondi, and Gregory C Beroza. Integrating deep neural networks with full-waveform inversion: Reparametrization, regularization, and uncertainty quantification. *Geophysics*, 87(1):1–103, 2021. [1](#)

Traversing within the Gaussian Typical Set –Supplementary Materials–

A. Gaussian Typical Set

The formal definition of a typical set is as follows.

Definition 1 (Cover & Thomas [14]) Let $p_X(x)$ be a distribution whose support is \mathcal{X} . The typical set $A_\epsilon^{(n)}$ is defined as the set of sequences $(x_1, x_2, \dots, x_n) \in \mathcal{X}^n$, $x_i \stackrel{i.i.d.}{\sim} p_X$ that satisfy

$$\left| H[X] + \frac{1}{n} \log p_X(x_1, \dots, x_n) \right| \leq \epsilon, \quad (17)$$

where $H[X]$ is the entropy of random variable X .

Now a random vector $\mathbf{x} \in \mathbb{R}^n \sim \mathcal{N}(\mathbf{0}, \sigma^2 \mathbf{I})$ can be factorized as i.i.d. random variables that are distributed as $\mathcal{N}(0, \sigma^2)$. Therefore, we can regard \mathbf{x} as an i.i.d. sequence and give the following definition:

Definition 2 (Gaussian Typical Set) A Gaussian typical set is the typical set $A_\epsilon^{(n)}$ of $\mathbf{x} \in \mathbb{R}^n \sim \mathcal{N}(\mathbf{0}, \sigma^2 \mathbf{I})$.

The following theorem guarantees that a typical sample from $\mathbf{x} \in \mathbb{R}^n \sim \mathcal{N}(\mathbf{0}, \sigma^2 \mathbf{I})$ resides in the Gaussian typical set with very high probability.

Theorem 1 (Cover & Thomas [14]) For every $\epsilon > 0$, the typical set has probability $P(A_\epsilon^{(n)}) > 1 - \epsilon$ with a sufficiently large dimension n .

These theoretical facts again justify our Gaussianization approach, which first makes each component as independent as possible and then shapes each component towards the same marginal 1D Gaussian distribution. As a result, the Gaussianization layers shape a latent vector towards a typical example from the desired high-dimensional isotropic Gaussian distribution.

B. More Details of the Gaussianization Layers

B.1. ICA Layer

The overall ICA layer is summarized in Algorithm 1. We set a maximum number of the fixed-point iterations to reduce computational cost and ensure accurate gradient computation that can pass the finite-difference convergence test. **Data Iterative Whitening.** The FastICA algorithm typically requires that the data are pre-whitened. After subtracting the mean, we use the following steps to whiten the data, which are also used later in ICA iterations to decorrelate column vectors in the orthogonal matrix [22]:

1. Compute

$$\mathbf{W} = \mathbf{W} / \sqrt{\|\mathbf{W}^\top \mathbf{C} \mathbf{W}\|_2} \quad (18)$$

2. Repeat until convergence

$$\mathbf{W} = \frac{3}{2} \mathbf{W} - \frac{1}{2} \mathbf{W} \mathbf{W}^\top \mathbf{C} \mathbf{W}, \quad (19)$$

where $\mathbf{C} = \mathbb{E}[\mathbf{v}_i \mathbf{v}_i^\top] + \eta \mathbf{I}$ is the data covariance matrix, to which we add a small constant (e.g., $\eta = 0.001$) on the diagonal entries to avoid ill-conditioning.

The Modified FastICA Iterations. As stated in [23], the objective function for one neural unit of the weight vector \mathbf{w}_i and input \mathbf{v} is

$$\begin{aligned} \arg \max_{\mathbf{w}_i} \mathbb{E} [\Phi(\mathbf{w}_i^\top \mathbf{v})], \\ \text{s.t., } \mathbb{E} [(\mathbf{w}_i^\top \mathbf{v})^2] = 1, \end{aligned} \quad (20)$$

where Φ is the contrast function (e.g., logcosh). The original derivations convert this constrained optimization to an unconstrained one using Lagrange multipliers. However, this procedure is unnecessary since the matrix \mathbf{W} is orthogonalized after each iteration, and the input vectors have been pre-whitened. Therefore, we only need to solve the following equation

$$\mathbb{E} [\mathbf{v} \phi(\mathbf{w}_i^\top \mathbf{v})] = 0, \quad (21)$$

whose Jacobian is

$$\begin{aligned} J &= \mathbb{E} [\mathbf{v} \mathbf{v}^\top \phi'(\mathbf{w}_i^\top \mathbf{v})] \\ &\approx \mathbb{E} [\mathbf{v} \mathbf{v}^\top] \mathbb{E} [\phi'(\mathbf{w}_i^\top \mathbf{v})] = \mathbb{E} [\phi'(\mathbf{w}_i^\top \mathbf{v})], \end{aligned} \quad (22)$$

where ϕ is the derivative of Φ . The Newton iteration scheme is thus

$$\mathbf{w}_i = \mathbf{w}_i - \mathbb{E} [\mathbf{v} \phi(\mathbf{w}_i^\top \mathbf{v})] / \mathbb{E} [\phi'(\mathbf{w}_i^\top \mathbf{v})]. \quad (23)$$

To improve the convergence, we damp the iterations by a parameter $\alpha \in (0, 1)$. Also, using the same technique to convert the Newton iterations to fixed-point iterations in [22, 23], we arrive at the modified fixed-point iteration scheme (Equation 9):

$$\mathbf{w}_i = \alpha \mathbb{E} [\mathbf{v} \phi(\mathbf{w}_i^\top \mathbf{v})] - \mathbb{E} [\phi'(\mathbf{w}_i^\top \mathbf{v})] \mathbf{w}_i, \quad (24)$$

followed by the aforementioned decorrelation procedure after each step.

Algorithm 1: ICA Layer

Input : data matrix $V \in \mathbb{R}^{D \times N}$ whose column vectors $\{\mathbf{v}_i\}, i = 1 \dots N$ are realizations of i.i.d. random vectors $\{\mathbf{v}_i\}, i = 1 \dots N$, respectively; error tolerance ϵ ; damping parameters: η and α ; maximum iteration numbers J and K .

Output: matrix $P \in \mathbb{R}^{D \times N}$ with i.i.d. entries

```
// Whitening stage
1  $V = V - \text{mean}(V, \text{dim} = 1)$ ,
   $C = \frac{1}{N-1} VV^\top + \eta I$ ;
2  $W \leftarrow I$ ;
3  $W_0 = W \leftarrow W / \sqrt{\|W^\top C W\|_2}$ ,  $k \leftarrow 1$ ;
4 while  $k \leq K$  do
5    $W \leftarrow \frac{3}{2} W - \frac{1}{2} W W^\top C W$ ;
6   if  $\|W - W_0\| < \epsilon$  then
7     break;
8    $W_0 \leftarrow W$ ,  $k \leftarrow k + 1$ ;
9  $V \leftarrow W^\top V$ ;
// ICA stage
10  $W = W^\dagger \leftarrow I$ ,  $j \leftarrow 1$ ;
11 while  $j \leq J$  do
12   Compute  $W$  using Equation 10;
13    $W = W_0 \leftarrow W / \sqrt{\|W^\top W\|_2}$ ,  $k \leftarrow 1$ ;
14   while  $k < K$  do
15      $W \leftarrow \frac{3}{2} W - \frac{1}{2} W W^\top W$ ;
16     if  $\|W - W_0\| < \epsilon$  then
17       break;
18      $W_0 \leftarrow W$ ,  $k \leftarrow k + 1$ ;
19   if  $\|W - W^\dagger\| < \epsilon$  then
20     break;
21    $W^\dagger \leftarrow W$ ,  $j \leftarrow j + 1$ ;
22 return  $P \leftarrow W^\top V$ .
```

The convergence of the modified FastICA iterations can be proved similarly as in [46]. Without the damping factor, it is required that

$$\mathbb{E}[b_i \phi(b_i) - \phi'(b_i)] \neq 0, \quad (25)$$

where $b_i, i=1, \dots, n$ are entries of the original random vector before mixing. If the distribution of b_i is a Gaussian, this condition is violated, corresponding to the fact that ICA cannot resolve Gaussian source vectors. Our introduction of α avoids this problem at the theoretical level.

B.2. Power Transformation Layer

We use a custom operator based on SciPy's implementation using Brent's algorithm [10] to find an approximate

Algorithm 2: Power Transformation Layer

Input : data vector \mathbf{p}

Output: Vector \mathbf{s} whose components are i.i.d.

- 1 Estimate λ from \mathbf{p} using Equation 12 ;
- 2 Compute \mathbf{s} with the estimated λ and data \mathbf{p} using Equation 11 ;
- 3 **return** \mathbf{s} .

minimum of Problem 12. Continuing from the approximate minimum, we use Brent's root finding algorithm [10] to find the minimum where the gradient vanishes. Since the parameter λ depends on input data, we need to back-propagate the gradient through the optimization process.

The power transformation layer is summarized in Algorithm 2.

B.3. Lambert W Layer

The transformation Equation 13 is bijective if $\delta \geq 0$, and we can use the Lambert W function to find its inverse. The Lambert W function W is defined as the inverse of $q = W^{-1}(t) = t \exp(t)$, where t and q are scalars. Given q , Halley's method can be used to find $t = W(q)$ [13]. Hence, the inverse of Equation 13 is

$$X = W_\delta \left(\frac{S - \mu_X}{\sigma_X} \right) \sigma_X + \mu_X, \quad (26)$$

where

$$W_\delta(u) = \text{sign}(u) \sqrt{\frac{W(\delta u^2)}{\delta}}. \quad (27)$$

We use the parameterized Lambert $W \times F_X$ distribution family to approximate a heavy-tailed input distribution and use Equation 26 to recover a distribution with lighter tails. In order to make the recovered distribution close to a Gaussian distribution, we compute the optimal heavy-tail parameter δ by minimizing the difference of the kurtosis of the output distribution and 3 (Kurtosis is a common surrogate measure of negentropy [24]):

$$\hat{\delta}_{\text{GMM}} = \arg \min_{\delta > 0} \left| \text{Kurt} \left(W_\delta \left(\frac{\mathbf{s} - \mu_X}{\sigma_X} \right) \right) - 3 \right|^2, \quad (28)$$

where \mathbf{s} is the data vector, and Kurt is the kurtosis. We constrain $\delta > 0$, and solve Equation 28 using the L-BFGS-B optimizer.

In addition, we estimate the mean μ_X and standard deviation σ_X along with δ using the Iterative Generalized Method of Moments (IGMM) [18], which embeds an optimization problem for δ in an outer loop of iterations to estimate σ_X and μ_X (see Algorithm 3). If the kurtosis of input data vector is not greater than 3, we skip the whole Lambert $W \times F_X$ layer by directly outputting the data vector.

Algorithm 3: Lambert $W \times F_X$ Layer with the Iterative Generalized Method of Moments (IGMM) [18]

Input : data vector \mathbf{s} , error tolerance ϵ

Output: vector \mathbf{x} whose empirical distribution is less heavy-tailed than \mathbf{s} , and its kurtosis ≈ 3)

- 1 Initialize: $\xi^{(0)} \leftarrow (\hat{\mu}_X^{(0)}, \hat{\sigma}_X^{(0)}, \hat{\delta}^{(0)})$, $k = 0$;
 - 2 Compute initial kurtosis $\beta_2 = \text{Kurt}(\mathbf{s})$;
 - 3 **if** $\beta_2 \leq 3$ **then**
 - 4 | return \mathbf{s} ;
 - 5 **end**
 - 6 **while** $k \leq K$ **and** $\|\xi^{(k)} - \xi^{(k-1)}\| \geq \epsilon$ **do**
 - 7 | $\mathbf{u}^{(k)} \leftarrow (\mathbf{s} - \mu_X^{(k)}) / \sigma_X^{(k)}$;
 - 8 | Compute $\delta^{(k+1)}$ using Equation 28;
 - 9 | $\mathbf{u}^{(k+1)} \leftarrow \mathbf{W}_{\delta^{(k+1)}}(\mathbf{u}^{(k)})$;
 - 10 | $\mathbf{x}^{(k+1)} \leftarrow \mathbf{u}^{(k+1)} \sigma_X^{(k)} + \mu_X^{(k)}$;
 - 11 | Update $\mu_X^{(k+1)} \leftarrow \mathbb{E}[\mathbf{x}^{(k+1)}]$, and $\sigma_X^{(k+1)} \leftarrow \sqrt{\text{Var}(\mathbf{x}^{(k+1)})}$;
 - 12 | $\xi^{(k+1)} \leftarrow (\hat{\mu}_X^{(k+1)}, \hat{\sigma}_X^{(k+1)}, \hat{\delta}^{(k+1)})$;
 - 13 | $k \leftarrow k + 1$;
 - 14 **end**
 - 15 **return** $\mathbf{x} = W_\delta \left(\frac{\mathbf{s} - \mu_X}{\sigma_X} \right) \sigma_X + \mu_X$,
-

C. Details of Training

For the deconvolution experiments, we split the 30000 images from CelebA-HQ into the subsets of training (24183 images), validation (2993 images), and testing (2824 images) following the original splits from CelebA [34]. These images were also downsampled to the resolution of 128×128 .

To construct the dataset of layer models, we created layer geometries by intersecting sine functions of randomly generated wavelengths, initial phases, and dip angles. Then, we generated an array of 20 numbers equally spaced between 0.1 and 0.9. Each layer picked one number a from the array with equal probability and sampled a value from the distribution $\mathcal{N}(a, 0.01^2)$ as the value of the layer. There are 16000, 4000, and 2000 examples in the training, validation, and testing sets. We used 100 randomly selected examples from the test set for inversion. We show 32 training and 32 generated examples in Figure 10.

For the hyper-parameters of the Glow networks, we used 4 multi-scale levels and 32 flow-steps for both CelebA-HQ and the layer models. As mentioned in the main text, we only used additive coupling layers. Figure 11 reports the training process. For each epoch, we computed the train-

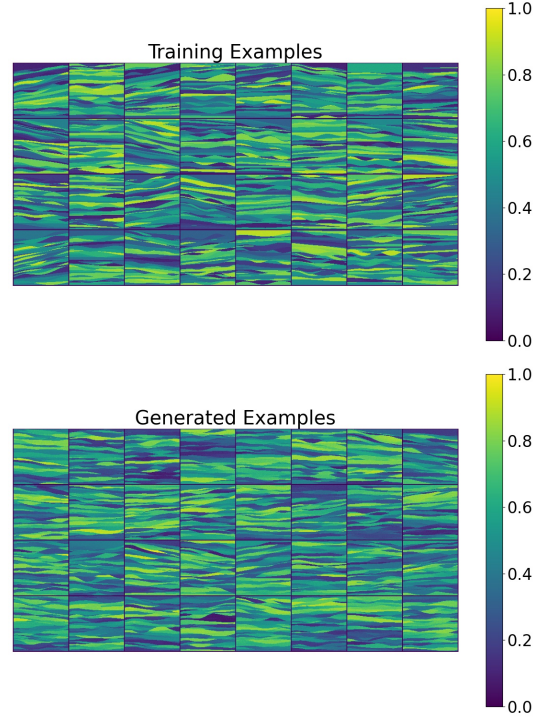


Figure 10. Training and generated examples of layer models. The temperature is set to 1.0.

ing negative log-likelihood (NLL) averaged throughout the epoch, and the validation NLL at the end of the epoch. For both CelebA-HQ and layer models, the validation curves suggest that it is better to use 4 multi-scale levels. We chose the network weights from the epoch before the validation NLL stopped to decrease: 850 for the CelebA-HQ dataset and 460 for the layer models. All training was conducted using 8×32 GB Nvidia V100 GPUs with a batch size of 64. We used the Adam optimizer [26] with a learning rate of $1e-4$, as well as $\beta_1 = 0.9$ and $\beta_2 = 0.99$.

D. Gradient Computation of the Optimization-based Differentiable Layers

In the power transformation and Lambert $W \times F_X$ layers, there are operators whose outputs are obtained by solving optimization problems formally described as

$$\mathbf{y} = \arg \min_{\mathbf{y}} l(\mathbf{x}, \mathbf{y}), \quad (29)$$

where l denotes the objective function that defines the operator, symbol \mathbf{y} stands for the output, a scalar in our cases but can also be a vector in general situations. The optimal condition is

$$l_{\mathbf{y}}(\mathbf{x}, \mathbf{y}) := L(\mathbf{x}, \mathbf{y}) = 0, \quad (30)$$

where the subscript denotes partial differentiation.

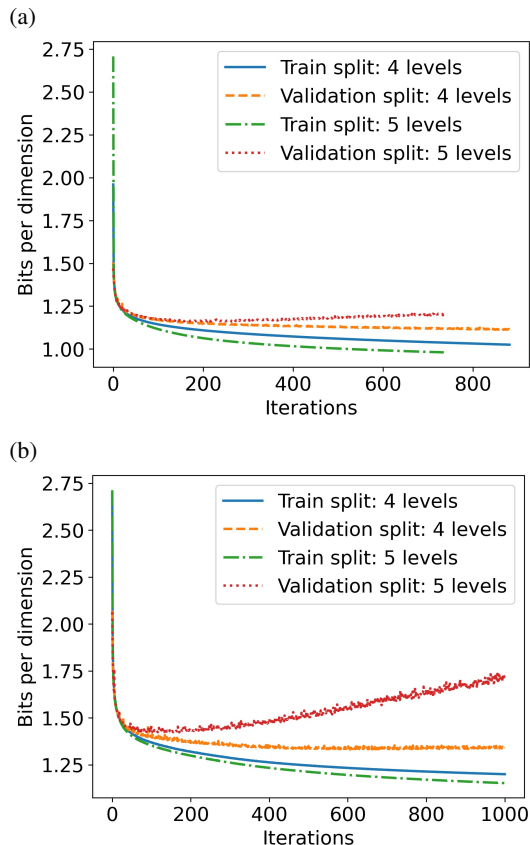


Figure 11. The negative log-likelihood or NLL (reported in bits per dimension) on the training and validation splits with different numbers of multi-scale levels. (a) CelebA-HQ; (b) Layer models.

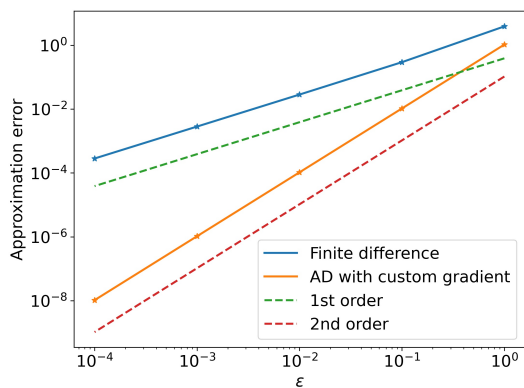


Figure 12. Gradient accuracy test for custom operators. An accurate gradient should make the error converge in the second order following the red dashed line.

The optimal condition implicitly defines a forward operator of the following form:

$$\mathbf{y} = \text{op}_{\text{forward}}(\mathbf{x}). \quad (31)$$

The backward operator is

$$\frac{\partial \chi}{\partial \mathbf{x}} = \text{op}_{\text{backward}}\left(\frac{\partial \chi}{\partial \mathbf{y}}, \mathbf{y}, \mathbf{x}\right), \quad (32)$$

where χ is the objective function of an inverse problem.

Differentiating Equation 30 with respect to \mathbf{x} , we have

$$L_{\mathbf{x}} + L_{\mathbf{y}}\mathbf{y}_{\mathbf{x}} = 0 \implies \mathbf{y}_{\mathbf{x}} = -L_{\mathbf{y}}^{-1}L_{\mathbf{x}}, \quad (33)$$

using the implicit function theorem. Then, to back-propagate the gradient from $\frac{\partial \chi}{\partial \mathbf{y}}$ to $\frac{\partial \chi}{\partial \mathbf{x}}$, we use

$$\frac{\partial \chi}{\partial \mathbf{x}} = \frac{\partial \chi}{\partial \mathbf{y}}\mathbf{y}_{\mathbf{x}} = -\frac{\partial \chi}{\partial \mathbf{y}}L_{\mathbf{y}}^{-1}L_{\mathbf{x}} = -\frac{\partial \chi}{\partial \mathbf{y}}H_{\mathbf{y}}^{-1}L_{\mathbf{x}}, \quad (34)$$

where $H_{\mathbf{y}}$ is the Hessian matrix of χ with respect to \mathbf{y} .

In our problems, the output \mathbf{y} is a scalar, so it is easy to use automatic differentiation to compute $L_{\mathbf{y}}$ directly and hence $L_{\mathbf{y}}^{-1}$. Otherwise, if \mathbf{y} has many parameters, we can first solve the following linear system with an auxiliary vector λ :

$$\lambda H_{\mathbf{y}} = -\frac{\partial \chi}{\partial \mathbf{y}}, \quad (35)$$

and then compute the gradient using

$$\frac{\partial \chi}{\partial \mathbf{x}} = \lambda L_{\mathbf{x}}, \quad (36)$$

a technique also known as the adjoint-state method. Note that there is no need to compute the Hessian explicitly, but one can use automatic differentiation to compute the vector-Hessian product $\lambda H_{\mathbf{y}}$ and utilize iterative linear solvers like GMRES [49] to solve the linear system.

As a final note, we check the accuracy of our gradient computation using the finite-difference convergence test based on Taylor expansion:

$$f(\mathbf{x} + \epsilon \delta \mathbf{x}) = f(\mathbf{x}) + \epsilon \nabla f(\mathbf{x})^{\top} \delta \mathbf{x} + \mathcal{O}(\epsilon^2), \quad (37)$$

where $\delta \mathbf{x}$ is a random vector with a unit ℓ_2 norm, and $\nabla f(\mathbf{x})$ is computed using our custom gradient. We here define f as a composite function that maps the (vector) output of an forward operator to a scalar, e.g., $f(\mathbf{x}) = \|\text{op}_{\text{forward}}(\mathbf{x})\|_2^2$. Once we decrease ϵ , we should see that the error term $f(\mathbf{x} + \epsilon \delta \mathbf{x}) - f(\mathbf{x}) - \epsilon \nabla f(\mathbf{x})^{\top} \delta \mathbf{x}$ decreases at a speed of second order. All our layers passed this test, as the example shown in Figure 12. This test should be conducted in double precision.

E. Miscellaneous Topics

E.1. Gaussian Annulus Theorem.

Theorem 2 ([7]) For a n -dimensional standard Gaussian, for any $\beta \leq \sqrt{n}$, all but at most $3e^{-c\beta^2}$ of the probability mass lies within the annulus $\sqrt{n} - \beta \leq |x| \leq \sqrt{n} + \beta$, where c is a fixed positive constant.

Bojanowski *et al.* [8] recognized this issue in their generative latent optimization processes and projected the latent vector onto a sphere. In addition to constraining the norm of latent vectors only, our approach Gaussianizes the latent vectors. In fact, a latent vector staying within the Gaussian annulus geometrically does not necessarily map to a plausible image. For example, all latent vectors in Figure 3 have almost the same ℓ_2 norm, but the uppermost one does not correspond to a meaningful normalizing flow output.

E.2. Duality of KL Divergence

As also shown in [48], the KL-divergence between two distributions does not change under a differentiable invertible transformation, so

$$D_{\text{KL}} [p_M^*(\mathbf{m}) \| p_M(\mathbf{m}; \theta)] = D_{\text{KL}} [p_Z^*(\mathbf{z}; \theta) \| p_Z(\mathbf{z})], \quad (38)$$

where p_M^* is the target distribution in the physical parameter space, and p_Z^* is the corresponding latent-space distribution under the normalizing flow. This means that minimizing the forward KL divergence in the M domain or physical parameter space is equivalent to minimizing the reverse KL-divergence in the Z domain or the latent space.

This fact and Theorem 1 imply that a well-trained normalizing flow maps samples from the target distribution into the Gaussian typical set with very high probability and vice versa.

E.3. The Rolling Operation

After applying one set of the Gaussianization layers to the latent tensor, it might be desirable to apply the layers to a different set of non-overlapping patches from the latent tensor at a second time. The rolling operation shifts the latent tensor in the horizontal and vertical directions by half of the patch size w before patch extractions. The values at the boundaries are wrapped around to the opposite sides. One can, for example, use the `torch.roll` command to implement this functionality.

E.4. Initial Model Projection for Eikonal Tomography.

The first step of inversion is to find the latent vector that has a minimum ℓ_2 distance to that of an initial model in the physical parameter domain, given the prior from the network. To this end, we solve the following optimization problems for a maximum of 100 iterations:

$$\arg \min_{\mathbf{z}} \|\mathbf{m}_0 - f(\mathbf{z})\|_2^2 - \beta (\log p_Z(\mathbf{z}) - \log |\det J_f(\mathbf{z})|), \quad (39)$$

and

$$\arg \min_{\mathbf{v}} \|\mathbf{m}_0 - f \circ h(\mathbf{v})\|_2^2 - \beta (\log p_Z(h(\mathbf{v})) - \log |\det J_f(h(\mathbf{v}))|), \quad (40)$$

where \mathbf{m}_0 is the vector representation of the initial physical property field $m_0(\mathbf{x})$. Note that this step is necessary since we find that an inversion usually gets stuck at the beginning if we directly start from the inverse of the initial model under the normalizing flow: $\mathbf{z}_0 = f^{-1}(\mathbf{m}_0)$ without the Gaussianization layers.